Research Square

Preprints are preliminary reports that have not undergone peer review.
They should not be considered conclusive, used to inform clinical practice,
or referenced by the media as validated information.

Long term assessment of Saharan Dust Events in the Eastern Mediterranean by Optical and Microphysical Aerosol Metrics

Konstantinos Granakis
National Centre of Scientific Research "Demokritos"
Maria I. Gini
National Centre of Scientific Research "Demokritos"
Prodromos Fetfatzis
National Centre of Scientific Research "Demokritos"
Stergios Vratolis
National Centre of Scientific Research "Demokritos"
Vasiliki Vasilatou
National Centre of Scientific Research "Demokritos"
Angelos Laoutaris
National Centre of Scientific Research "Demokritos"
Manousos Ioannis Manousakas
National Centre of Scientific Research "Demokritos"
Christos Tzanis
National and Kapodistrian University of Athens
Konstantinos Eleftheriadis
elefther@ipta.demokritos.gr

National Centre of Scientific Research "Demokritos"

Article

Keywords:

Posted Date: August 25th, 2026

DOI: https://doi.org/10.21203/rs.3.rs-10716294/v1

License: This work is licensed under a Creative Commons Attribution 4.0 International License.
Read Full License

Additional Declarations: No competing interests reported.

Long term assessment of Saharan Dust Events in the Eastern Mediterranean by Optical and Microphysical Aerosol Metrics

K. Granakis[1,2], M. I. Gini[1], P. Fetfatzis[1], S. Vratolis[1], V. Vasilatou[1], A. Laoutaris[1], M.I Manousakas[1], C.G Tzanis[2] and K. Eleftheriadis[1]

[1]ENvironmental Radioactivity & Aerosol Technology for atmospheric & Climate ImpacT Lab, INRASTES, NCSR Demokritos, 15310 Ag. Paraskevi, Attica, Greece

[2]Climate and Climatic Change Group, Section of Environmental Physics and Meteorology, Department of Physics, National and Kapodistrian University of Athens, Athens, Greece

Correspondence to: K. Granakis and K. Eleftheriadis:
k.granakis@ipta.demokritos.gr and eleftheriadis@ipta.demokritos.gr

Abstract

Saharan dust events (SDEs) are among the most important natural aerosol phenomena influencing atmospheric composition, air quality, and regional climate across the Mediterranean. Their reliable detection in urban environments remains challenging due to the coexistence of anthropogenic fine-mode aerosols. In this study, SDEs are investigated at an urban background station in Athens, Greece, by combining in situ measurements of aerosol optical properties with particle size distribution data. The analysis includes scattering and absorption coefficients, single scattering albedo (SSA), scattering and absorption Ångström exponents (SAE, AAE), the single scattering albedo Ångström exponent (SSAAE), and the coarse-to-total volume ratio (CV/TV), with the coarse mode defined as particles with diameters greater than 1 μm. The performance of these indicators is evaluated against independent dust references from the SKIRON model and XRF elemental composition analysis. Among the examined criteria, the CV/TV > 0.70 threshold exhibits the most balanced performance, achieving high detection efficiency (~88%) with relatively low false positive rates (~20%). Event classification distributions and ROC analysis further support the reliability of this threshold for SDE classification across temporal scales. In contrast, SSAAE and SAE provide complementary insight into dust optical properties but are more strongly affected by anthropogenic aerosol influence, which can reduce their detection efficiency when dust is mixed with fine pollution particles. Overall, the results show that combining optical and microphysical parameters enhances the reliability of near-real-time SDE detection, particularly in urban environments affected by dust–anthropogenic pollution mixtures, and provides useful observational constraints for model validation and climatological assessment of dust transport over the Eastern Mediterranean and similar environments.

1. Introduction

Atmospheric aerosols play a major role in our environment, influencing both air quality and human health[1], while also perturbing the Earth's radiative balance. This occurs either directly, by altering the scattering and absorption of incoming solar radiation (short wavelengths) and outgoing terrestrial radiation (long wavelengths), or indirectly, by acting as cloud condensation nuclei that modify the microphysical and optical properties of clouds[2,3]. Dust outbreaks also influence radiative forcing at both regional and global scales which is generally expected to be negative[4]. The direct radiative forcing associated with dust varies globally between -0.3 and +0.1 W/m^2 [5]. According to Kaskaoutis et al.[6], the impact on radiative balance over Greece during the intense dust storm of March 2018 was estimated at the surface between -40 W/m^2 to -50 W/m^2 while at the top of atmosphere it ranged between -5 W/m^2 to -30 W/m^2. Furthermore, mineral dust affects the local rain/snow acidity as well as marine biochemical processes[7].

Globally, natural sources dominate ambient aerosol emissions, accounting for 98% of primary and secondary particle emissions. Among these, mineral dust is the second most abundant component (13%), following sea spray (84%)[8]. Saharan and Sahel deserts are the world's largest sources of airborne dust, contributing to up to 50-70% of the global dust emissions[9,10]. The Mediterranean Basin is frequently affected by Saharan dust intrusions, which are characterized by increased concentrations of coarse airborne particles. The increased dust concentrations during extreme Sahara dust events (SDE) may lead to exceedances of the daily PM_{10} limit values in many Southern European countries, such as Greece, Spain, and Italy[11,12,13]. A methodology for the quantification of the net African dust load in air quality monitoring networks was introduced in order to account for these events separately from exceedances due to anthropogenic emissions in urban areas. Specifically in Athens, the average contribution of Sahara dust to PM_{10} mass concentrations is in the order of 20-30%[14,15].

Recent epidemiological studies[16,17] suggest that desert dust storm events may pose significant health risks, as the average PM deposited mass in the upper and lower human respiratory tract is higher during days affected by Sahara dust (SD) intrusions than during non-SD days[14]. Dust particles may act as carriers of anthropogenic pollutants such as organics, sulphate, nitrate, ammonium, black carbon (BC), and trace and heavy metals, which in turn enhance the toxicity of local ambient aerosol[18,19]. Given the recent increasing trend in chemical tracers of dust reported

by Vasilakos et al.[20], identifying and quantifying these events has become increasingly critical for air quality management. While the established methodology introduced by Querol et al.[18] is widely utilized by environmental agencies to identify and exclude natural dust contributions from PM10 concentration exceedances, the optical and microphysical parameters evaluated here can serve as an additional, statistically robust assessment tool to complement such chemical-based approaches.

In this study, multiple metrics for identifying Saharan dust events were evaluated by examining specific optical and physical properties of atmospheric aerosols in a suburban Mediterranean environment in Greece. Specifically, we evaluated the single scattering albedo (SSA), scattering Ångström exponent (SAE), absorption Ångström exponent (AAE), and single scattering albedo Ångström exponent (SSAAE). These intensive optical properties are independent of particle mass. Additionally, aerosol number size distributions were used to estimate the aerosol coarse-to-total volume ratio (CV/TV). The study period covers the years 2015, 2017 and 2020, which provided the most extensive data coverage from the instruments used. Each parameter was assessed for its ability to identify Sahara dust events, and the results were compared against events identified through air mass back-trajectory analysis and dust forecasts. A complementarily evaluation was also performed for 2024 to assess the robustness of the results obtained in earlier years, using aerosol elemental composition as an independent reference for SDE identification.

2. Experimental

2.1 Sampling site

Continuous measurements of a number of aerosol parameters were performed at the Athens - Demokritos station (DEM station), member of GAW and part of the ACTRIS and PANACEA infrastructures (37.995° N, 23.816° E, 270 m a.s.l), which is located within the National Centre for Scientific Research “Demokritos” campus (Figure 1). This station lies at a suburban zone at the northeast corner of the Athens Metropolitan area on the hillside of Hymettus Mountain. The site is mainly influenced by the outflow of the urban emissions within the Athens valley area and occasionally by incoming air from the northeast, representative of regional atmospheric aerosols conditions[21,22].



Figure 1: The Demokritos Atmospheric Aerosol Measurement station in Athens, Greece. The maps were obtained from Google Maps (maps.google.com).

2.2 Instrumentation

The aerosol absorption coefficient (σ_{ap}) was obtained by 7-wavelength aethalometer (Rack Mount Aethalometer Model AE31, Magee Scientific Core, Berkeley, CA, USA) for seven wavelengths (370, 470, 520, 590, 660, 880 and 950nm). The instrument sampled aerosol through a PM_{10} cut-off inlet and recorded attenuation coefficients with 5 minutes temporal resolution. σ_{ap} was calculated by the following equation[23]:

$$\sigma_{ap} = \frac{A}{Q} \times \frac{\Delta ATN}{\Delta t} \cdot \frac{1}{C} \quad (1)$$

Where Q the volumetric flow rate, ΔATN is the change in attenuation during the time interval Δt, A is the filter spot area and C is the empirical constant that was used to correct for multiple scattering by the filter fibers and the scattering of the aerosol embedded in the filter. The value of 3.5 was used for C according to Zanatta et al.[24]. A correction with parameter R(ATN), which is associated with the shadowing effect and is estimated for each wavelength λ, was also applied[25]. This parameter depends on the number of particles embedded in the filter and is calculated as follows[23]:

$$R(ATN) = \left(\frac{1}{f} - 1\right)\frac{\ln(ATN) - ln10}{ln50 - ln10} + 1 \quad (2)$$

For values ATN below or equal to 10 the parameter R(ATN) was set equal to 1. Parameter f was calculated as: $f = \alpha(1 - \omega_0) + 1$ (3)

Where α is a constant parameter varying in the range (0.82-0.88) for the different wavelengths (950-370 nm) and ω_0 is the aerosol single scattering albedo.

Aerosol light scattering (σ_{sc}) and backward scattering (σ_{bsc}) coefficients were retrieved by a LED-based integrating nephelometer (model Aurora 3000, ECOTECH Pty, Ltd, Victoria, Australia) operating at three different wavelengths (450, 525 and 635nm) with time resolution of 1 minute. The scattering coefficients were corrected for the truncation error following the procedure described in Müller et al.[26].

The Grimm (Model, 107@660 nm laser light wavelength) optical particle counter (OPC) provides the particle size distribution in the size range from 0.25 μm to 32μm. The OPC demonstrated counting accuracy within 10% for the size range of 0.25 μm to 1 μm according to the comparison at WCCAP (World Calibration Centre for Aerosol Physics) (Vratolis et al., 2017). The instrument was operated continuously with temporal resolution 1 minute.

The Laser Aerosol Spectrometer (LAS, Model 3340A, TSI Inc.) was additionally employed to obtain particle size distributions during 2024. The instrument measures aerosol particles over a wide size range, from approximately 0.09 μm to 10 μm, using a 660 nm laser source and a single-particle light scattering detection principle. The LAS operated continuously throughout the measurement period with a temporal resolution of one minute. According to the manufacturer's specifications, the instrument provides high counting accuracy and reproducibility across its full measurement range, making it suitable for both ambient and laboratory aerosol characterization. All instruments were sampling under dry conditions (RH< 40%) in accordance with the ACTRIS recommendations.

$PM_{2.5}$ and PM_{10} samples were collected on Teflon and Quartz fiber filters, by the use of a low-volume samplers. Filters are weighed using a Sartorius BP211D microbalance, at controlled conditions of relative humidity and temperature (T=19-21 C° & RH=45-50%). The elemental composition of the collected aerosol samples was analyzed by energy-dispersive X-ray

fluorescence (EDXRF) spectroscopy using a PANalytical Epsilon 5 secondary target system. The calibration methodology and the evaluation of analytical uncertainties have been comprehensively described in previous works[27,28].

All data reported were normalized to standard conditions (273 K, 1013 hPa).

2.3 Data analysis

2.3.1 Optical properties

Based on that scattering and absorption coefficients (extensive optical parameters), the following intensive optical parameters were determined:

a. The SAE depends on physical properties of aerosol and mainly is inversely related to the size of particles. Namely, the larger particles correspond to the smaller exponent and vice versa. Generally, small values of SAE ($SAE_{450\text{-}635}<1$) indicate a predominance of coarse particles while $SAE_{450\text{-}635}>1.5$ indicates a predominance of fine particles[29,1]. SAE was estimated for each pair of wavelengths by following equation[30]:

$$SAE_{\lambda 1,\lambda 2} = -\frac{log\left(\frac{\sigma_{sc,\lambda_1}}{\sigma_{sc,\lambda_2}}\right)}{log\left(\frac{\lambda_1}{\lambda_2}\right)} \quad (4)$$

b. The AAE is related to the chemical composition and material properties of atmospheric aerosol. Generally, high values of AAE (AAE≥2) correspond to BrC for small particles or mineral dust in the case of large particles[31]. Conversely, low values of AAE (AAE≈1) correspond to BC that absorbs radiation across the whole solar spectrum with the same efficiency[1]. The AAE was derived from the following equation:

$$AAE_{\lambda 1,\lambda 2} = -\frac{log\left(\frac{\sigma_{ap,\lambda_1}}{\sigma_{ap,\lambda_2}}\right)}{log\left(\frac{\lambda_1}{\lambda_2}\right)} \quad (5)$$

c. The Extinction Ångström Exponent (EAE) reflects the wavelength dependence of total light extinction (the sum of scattering and absorption) and, similarly to SAE, is standardly used to provide a qualitative indication of the dominant aerosol particle size. EAE was calculated across the selected wavelength pairs using the following relationship:

$$EAE_{\lambda 1,\lambda 2} = -\frac{log\left(\frac{\sigma_{ext,\lambda_1}}{\sigma_{ext,\lambda_2}}\right)}{log\left(\frac{\lambda_1}{\lambda_2}\right)} \quad (6)$$

d. The SSA is defined as the ratio of scattering (σ_{sc}) and extinction (σ_{ext}) coefficients with the last to be the sum of absorption and scattering coefficients[32].

$$SSA = \frac{\sigma_{sc}}{\sigma_{ext}} = \frac{\sigma_{sc}}{\sigma_{sc}+\sigma_{ap}} \quad (7)$$

Based on the above definition, the values of SSA ranges from 0 to 1 for completely absorbing particles and for puring scattering particles, respectively. Furthermore, SSA plays an important role in the Earth's radiative budget because non-absorbing particles provoke negative radiative forcing (cooling) in contrast to aerosol light absorption that can cause warning for strongly absorbing and low SSA aerosols.

e. The wavelength dependence of the SSA is called as SSAAE and it is described as[1]:

$$SSAAE = (1 - SSA) \cdot (SAE - AAE) \quad (8)$$

This parameter provides general information about physical and chemical properties of aerosol, and according to Collaud Coen et al.[7] , SSAAE is a good indicator for the presence of mineral dust in the atmosphere and in fact at the alpine station Jungfraujoch this parameter was able to detect 100% of SDE compared to other optical properties.

2.3.2 Number and volume size distribution measurements

The number size distributions obtained from the OPC were converted into volume size distributions (Figure S1). Subsequently, the coarse-to-total volume ratio (CV/TV) was calculated as a parameter for detecting Sahara dust events. The total aerosol volume was estimated by summing the aerosol volume concentrations across each size bin, up to 10 μm, as measured by the OPC. The same procedure was applied to calculate the total coarse volume concentration, defined as the sum of the volume concentrations for all size bins larger than 1 μm and up to 10 μm.

2.3.3 Air mass trajectory analysis and dust forecasts

To investigate the origins of the air masses arriving at the DEM station and to identify the days characterized as SDEs, we employed two models: the Hybrid Single-Particle Lagrangian Integrated Trajectory model (HYSPLIT)[33] and FLEXTRA[34]. These models simulate the long-

range and mesoscale transport of tracers from point or area sources, using interpolated measured or modeled meteorological fields and accounting for atmospheric processes such as diffusion and dry and wet deposition. Three-dimensional trajectories were computed for the sampling location (DEM station, 37.995° N, 23.816° E). HYSPLIT calculations were performed at 500, 1000, 2000 m a.s.l for 96-h backward trajectories, while the FLEXTRA model produced 7-day backward trajectories at three heights: 500, 1000, and 1500 m a.s.l. Additionally, dust concentration reanalysis data were obtained from the Skiron/Dust forecast model, with values provided for the surface (276.58 m a.s.l) and for three additional heights (454.22, 596.23 and 758.62 m a.s.l)[35].

3. Results and discussion

3.1 Overview of Aerosol Optical Properties

The aerosol optical properties measured at the DEM station provide a detailed characterization of urban background aerosol and its temporal variability during the study period, reflecting contributions from both locally emitted and regionally transported particles. At 525 nm, the scattering coefficient (σ_{sc}) averaged 44.55 ± 28.09 Mm^{-1}, with a median value of 39.14 Mm^{-1}, whereas the absorption coefficient (σ_{ap}) averaged 5.20 ± 3.62 Mm^{-1}. The corresponding mean single scattering albedo (SSA) was 0.89 ± 0.19, indicating the predominance of light scattering, although confirming contribution of absorbing aerosol to the overall aerosol optical response. These specific values are in close agreement with the long-term aerosol optical climatology reported for the DEM station by Granakis et al.[36], supporting the temporal representativeness of the observations. The observed optical signature reflects the combined influence of local anthropogenic emissions (e.g., traffic and residential heating) and natural aerosol sources, such as long-range transport of mineral dust.

To further characterize the temporal evolution of aerosol optical properties during the current study period, the monthly variability of key parameters is presented in the Figure S2. The scattering coefficient exhibits its highest values during spring and summer, reflecting the combined influence of Saharan dust intrusions and enhanced secondary aerosol formation under warmer and more photochemically active conditions. In contrast, the absorption coefficient peaks in winter, primarily due to increased emissions from residential heating and traffic, together with their accumulation under stable atmospheric conditions and reduced boundary-layer mixing. The

scattering Ångström exponent (SAE) is higher values in summer, indicating a greater contribution from fine-mode particles, whereas lower values in spring are consistent with an enhanced coarse-mode contribution associated with mineral dust transport. The seasonal variability of the single-scattering albedo (SSA) follows a similar pattern, with the highest values observed in summer, when scattering aerosol components predominate. These characteristic temporal patterns, also documented in the long-term climatological analysis of Granakis et al.[36], provide useful context for identifying and interpreting short-term aerosol episodes, particularly Saharan dust events (SDEs), and for assessing their influence on aerosol optical properties at the DEM station.

3.2 Case study: Optical and physical aerosol properties of a typical Sahara dust event

The number size distributions exhibit characteristic patterns that reflect the influence of different aerosol sources. Particles with diameters smaller than 2.5 μm are typically classified as fine aerosols, whereas those larger than 2.5 μm are considered coarse particles. However, previous studies have shown that the $PM_{2.5}$ fraction does not always represent a clear separation between fine and coarse modes. In the Eastern Mediterranean, the $PM_{1\text{-}2.5}$ range corresponds to the lower tail of the coarse mode in the mass size distribution, indicating that part of the $PM_{2.5}$ mass may include particles of mineral origin similar to those in the coarse fraction[14,37]. This is supported by Diapouli et al.[15], who reported concurrent increases in both $PM_{2.5}$ and PM_{10} during SDEs.

According to Conte et al.[38], the maximum contribution of Saharan dust is typically observed in the 2.5–3 μm size range, although this depends strongly on the source region. Specifically, dust originating from western Africa is associated with larger modal diameters (~5.6 μm), whereas eastern Saharan sources exhibit smaller characteristic diameters (~3.1 μm)[14]. The resulting size distribution during SDEs is therefore site-dependent and influenced by atmospheric processing during transport. Dry and wet deposition selectively remove particles of different sizes, while local emissions further modify the observed size distribution, particularly in urban environments.

SDEs are generally characterized by a decrease in SAE due to the dominance of coarse particles and an increase in AAE, driven by enhanced absorption in the UV spectrum associated with iron oxides in mineral dust[1]. However, under conditions of weak dust transport combined with significant anthropogenic influence, this characteristic optical signature may be altered. In such cases, SAE may exceed 1.5 while AAE decreases below ~1.3, leading to positive SSAAE values.

This behavior reflects the increasing contribution of fine particles from combustion sources. When mineral dust is internally or externally mixed with black carbon (BC), the spectral dependence of absorption is often dominated by BC, effectively masking the dust signal in optical measurements.

Accordingly, SDE detection can be based on the spectral dependence of the single scattering albedo (SSA), commonly expressed through the SSA Ångström exponent (SSAAE)[7]. Under coarse-mode dominance, scattering approaches the geometric optics regime (i.e. scattering is controlled mainly by particle size and shape), resulting in weak wavelength dependence. Consequently, SAE becomes smaller than AAE, leading to negative SSAAE values (Eq. 8). In contrast, when fine particles dominate, scattering decreases more rapidly with wavelength than absorption, resulting in positive SSAAE values[39]. This framework provides a physically consistent basis for interpreting aerosol optical behavior under mixed atmospheric conditions.

Figure 2(a–d) presents the temporal evolution of scattering (σ_{sc}), absorption (σ_{ap}), extinction (σ_{ext}), and SSA during the SDE (13–15 May 2017), which is considered a representative high-intensity Saharan dust event. Figure S3 shows the air mass back-trajectories derived from the HYSPLIT simulations. As illustrated, the air masses reaching Athens on 14 May 2017 originated from northwestern Africa, including Libya, Algeria, Morocco and Mauritania, deep within the Saharan desert. The scattering coefficient exhibits a pronounced increase during the event, closely followed by the extinction coefficient. In contrast, absorption shows only a moderate enhancement, primarily during the peak of the episode. Both scattering and extinction display a reversal in their spectral dependence (i.e., reduced wavelength dependence), consistent with coarse particle dominance. Conversely, absorption exhibits a stronger wavelength dependence during the event. SSA approaches unity during the SDE, reflecting the predominance of scattering over absorption, and shows an inversion pattern with higher values at longer wavelengths.

Figure 3 presents the temporal evolution of the Ångström exponents along with the CV/TV ratio derived from OPC measurements, and dust concentrations from the Skiron model. During the SDE, SAE and EAE show a clear decrease, with values ranging between −0.8 and 0.5, compared to typical background values between 1 and 2.5. The AAE remains relatively stable (~1.2), with occasional increases up to 1.6. In contrast, $AAE_{370\text{-}590}$ exhibits enhanced sensitivity, showing a more pronounced increase during the event, likely reflecting stronger absorption at shorter wavelengths due to dust composition. At the same time, SSAAE values become negative (-0.05 to

-0.2), while the CV/TV ratio increases significantly, reaching values up to 0.8. The concurrent behavior of these parameters provides a clear signature of Saharan dust presence, linking optical properties with particle size characteristics.

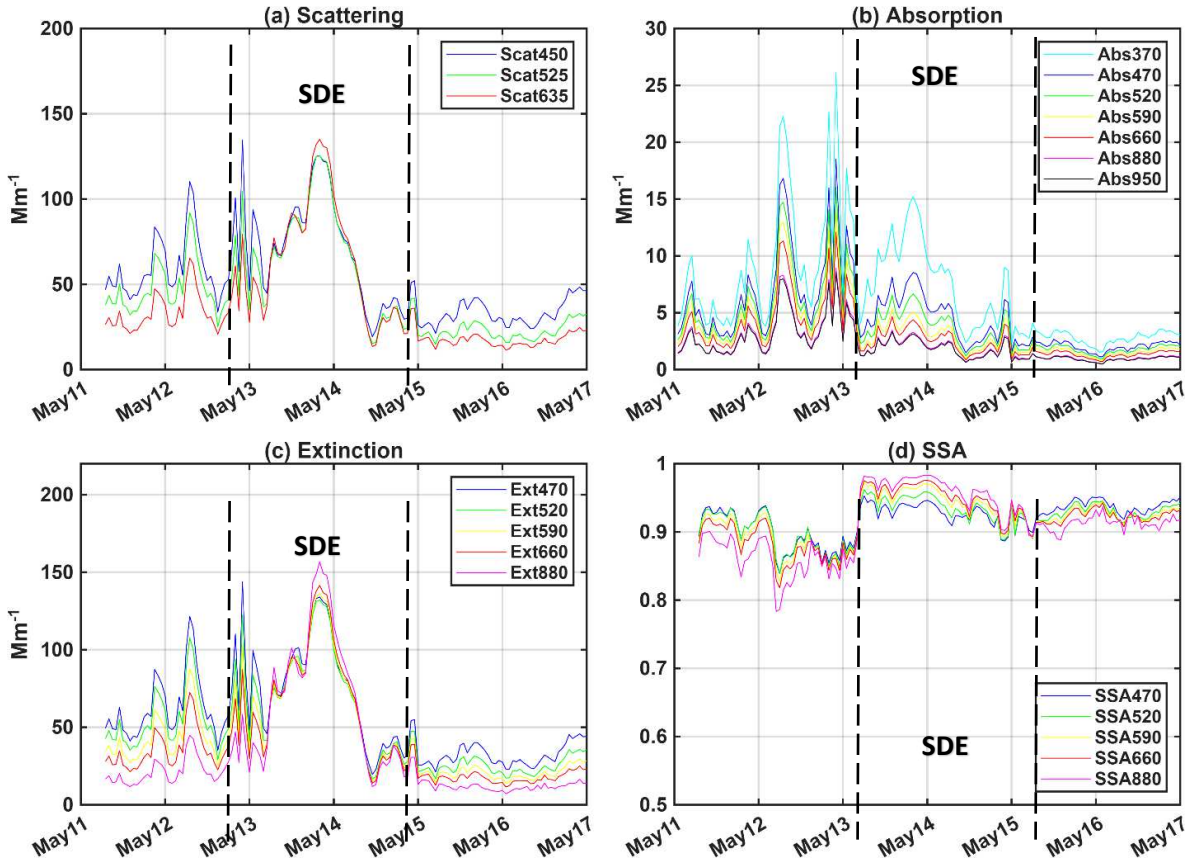


Figure 2. Time evolution (1 hourly averages) of (a) scattering, (b) absorption, (c) extinction coefficients and (d) SSA during SDE (13.05.2017 - 15.05.2017).

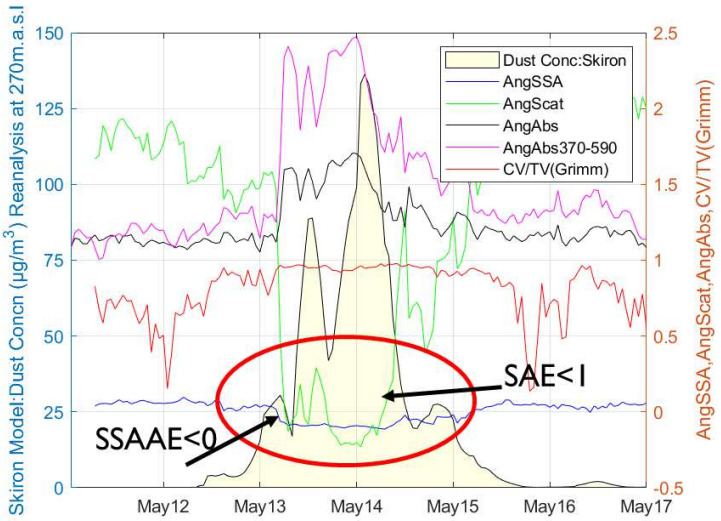


Figure 3. Temporal evolution of Angstrom exponents (SAE, AAE, $AAE_{370-590}$, EAE and SSAAE), ratio CV/TV derived by OPC (Grimm) as well as reanalysis data of dust concentration (µg/m^3) by Skiron model for SDE (13.05.2017 - 15.05.2017).

Additionally, the average volume size distributions (dV/dlogDp) of ambient aerosols were calculated from the OPC number size distributions for both Saharan Dust Event (SDE) and non-SDE cases throughout the study period (Figure S4). Modal analysis of the volume distributions shows that particles between 1 and 2.5 µm fall within the second lognormal mode, corresponding to the coarse mode with an optical median diameter of around 4 µm. This finding supports the use of 1 µm as the size threshold for distinguishing between fine and coarse modes. Furthermore, the average dust contribution to the total aerosol volume during the SDE was estimated at approximately 44%. These results align with recent studies conducted in southeastern Italy (Lecce)[38]. As demonstrated in earlier research, intense SDEs are associated with low $PM_{2.5}/PM_{10}$ ratios (<0.4) in filter samples, particularly when the net dust load exceeds 10 µg/m³ at the DEM station[15]. Therefore, the CV/TV ratio can serve as a reliable tracer for detecting Saharan dust events. For the specific case studied here, the CV/TV ratio was measured as 0.95 ± 0.02.

3.3 Statistical Assessment of SDE Identification Metrics

As discussed above, SDEs can be detected using aerosol optical property measurements, which capture the changes induced by mineral dust in the spectral dependence of aerosol scattering and absorption[7]. Figure 4a presents the SAE–AAE scatter plot (Ångström matrix), color-coded by CV/TV ratio, while Figure 4b present the same matrix, colored coded according to SDE occurrence, defined as days with SKIRON dust concentrations above 10 µg m^{-3}. This specific

threshold was empirically selected to account for the tendency of regional models to occasionally overestimate surface dust concentrations. This relative conservative criterion reduces the likelihood of including borderline cases or background variability, thereby increasing confidence in the identification of distinct Saharan dust intrusions.

SDE conditions are typically characterized by reduced SAE values, reflecting the dominance of coarse particles, together with enhanced AAE values, indicative of stronger absorption at shorter wavelengths by mineral dust. Accordingly, lower SAE values combined with elevated AAE generally correspond to higher CV/TV ratios and dust-dominated conditions. However, a substantial fraction of SDE cases falls outside the traditionally defined dust regime, including points with SAE values exceeding 1.5 and AAE values below 1.3. These cases are generally associated with relatively low dust contributions (CV/TV < 0.4), suggesting weaker or mixed dust influence. Conversely, some cases with high CV/TV ratios exhibit optical properties that do not display a classical dust signature. This behavior may be attributed to the co-presence of fine anthropogenic particles, which can modify the optical response of mineral dust, particularly in an urban environment. These findings highlight the added value of incorporating the CV/TV ratio for identifying low-intensity or optically masked dust events that may not be adequately captured by traditional Ångström-based criteria.

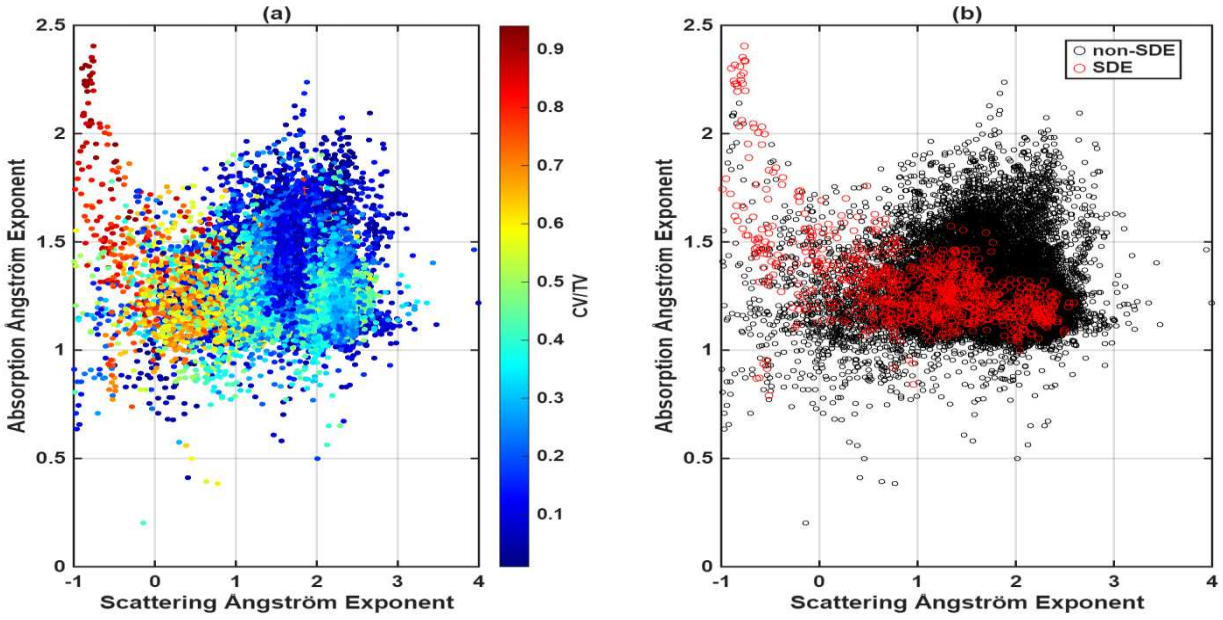


Figure 4. Scatter plots of AAE vs. SAE weighted by coarse fraction CV/TV (a) and Scatter plot of AAE vs. SAE weighted by the occurrence of SDEs (b), for three indicative years.

Table 1 summarizes the basic statistical parameters, namely the mean and standard deviation, of the intensive optical properties and the CV/TV ratio under both SDE and non-SDE conditions. Overall, under SDE conditions, mean SAE and EAE values are below unity, while mean SSAAE values are negative. In contrast, non-dust conditions are characterized by significantly higher SAE and EAE values, both averaging 1.7, together with positive SSAAE values. Mean AAE values are comparable between SDE and non-SDE conditions, although $AAE_{370-590}$ is slightly higher, suggesting enhanced sensitivity to absorption in the UV range. The CV/TV ratio shows a pronounced increase during SDEs, with mean values approaching or exceeding 0.70.

In addition, Figures 5a and 5b illustrate the SSAAE - SAE scatter plot, color coded by CV/TV ratio and SDE occurrence, respectively. This approach provides a clear depiction of the transition between fine- and coarse-mode dominated conditions. The majority of cases characterized by low SAE and negative SSAAE, indicative of mineral dust dominance, are associated with elevated CV/TV ratios. Nevertheless, a non-negligible number of points with positive SSAAE and relatively high SAE also correspond to increased coarse fractions. These cases are primarily linked to mixed aerosol conditions, where mineral dust coexists with anthropogenic fine particles, leading to a partial masking of the dust optical signature.

Under intense SDE conditions, both the SAE and SSAAE criteria successfully detect the presence of dust in nearly all cases. However, during weaker dust transport events, particularly when accompanied by elevated urban pollution levels, these optical indicators may fail to capture the presence of mineral dust. In contrast, the CV/TV ratio remains sensitive to the enhanced contribution of coarse particles, even under mixed conditions. This behavior highlights its robustness as a key parameter for detecting SDEs in complex atmospheric environments.

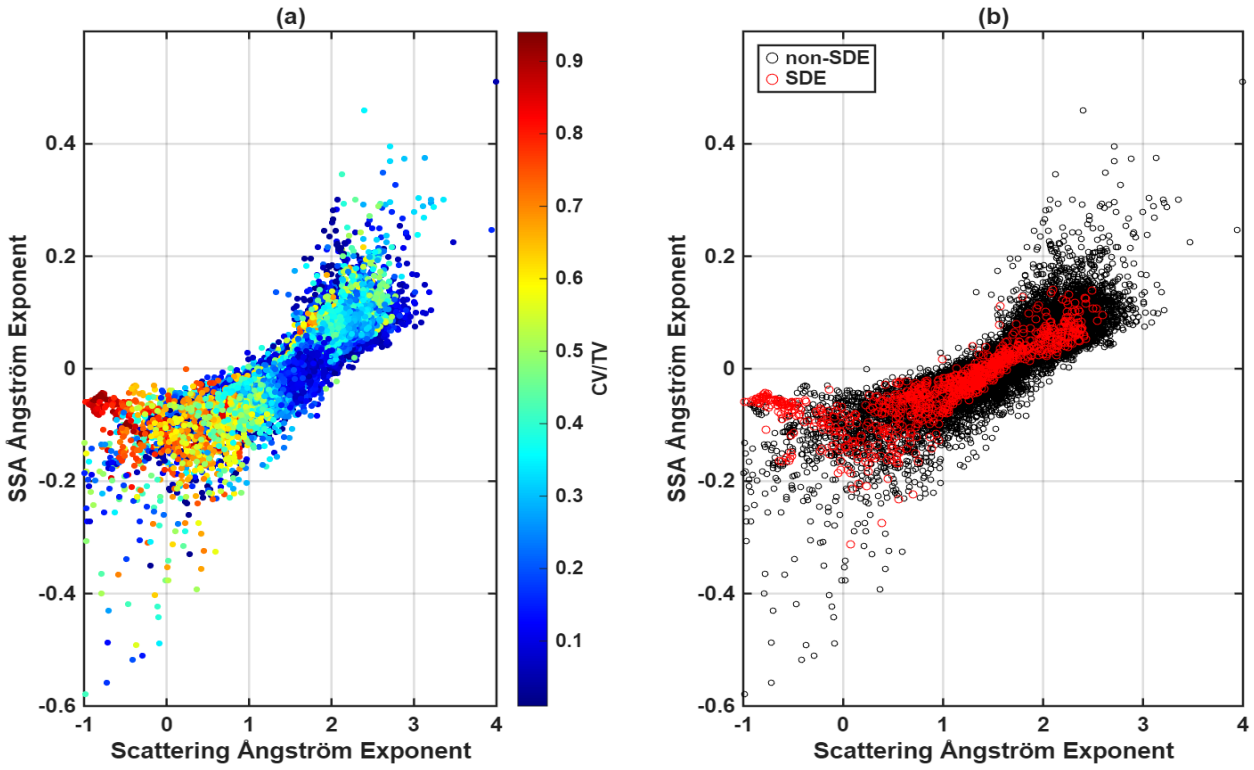


Figure 5. Scatter plots of SSAAE vs. SAE weighted by coarse fraction CV/TV (a) and Scatter plot of AAE vs. SAE weighted by the occurrence of SDEs (b), for three indicative years.

Based on above analysis, three criteria are proposed for SDE detection: SSAAE < 0, SAE < 1, and CV/TV > 0.70. The EAE exhibits behavior similar to SAE and can therefore be considered equivalent. While SSAAE has been shown to be a reliable indicator of SDE in remote or background environments[7], its applicability in urban settings may be limited by the influence of fine anthropogenic particles. The combined use of multiple metrics, particularly the inclusion of independent microphysical information such as the CV/TV ratio together with optical metrics, is essential for robust SDE detection under real-world conditions.

3.4.1 Evaluation of Optical and Microphysical Metrics for Saharan Dust Event Identification

In this study, SKIRON dust concentration forecasts were used as a reference for SDE occurrence, with a dust concentration threshold of 10 μg m^{-3}. Based on this reference, we further assessed the performance of individual metrics (SAE < 1, SSAAE < 0, and CV/TV > 0.70), as well as their combinations, focusing on events for which all parameters were simultaneously available.

Specifically, the true positive rate was evaluated for each individual metric and for different combinations of criteria, whereby a day was classified as an SDE if at least one, at least two, or all

three criteria were satisfied (Table 2). The results show that the individual SAE and SSAAE metrics detected 41% and 57% of Saharan dust events, respectively. In contrast, the CV/TV parameter exhibited substantially higher sensitivity, identifying 80% of the cases. The false positive rate was also evaluated (Table 3), defined as the fraction of cases in which an SDE was indicated by the metrics but not confirmed by the reference classification. SAE showed the lowest false positive rate (14%), followed by CV/TV (20%) and SSAAE (29%). False positive SDE are likely associated with local dust sources, including the resuspension of soil particles from urban surfaces such as road networks and construction sites.

Among the tested combined criteria, the "at least one criterion identifies an SDE" scenario yields the highest detection efficiency, albeit at the expense of an increased false positive rate. Conversely, requiring all three criteria to be satisfied results in a negligible false positive rate but significantly reduces the overall detection capability to 40%, underscoring the importance of balancing detection sensitivity and classification specificity.

The findings of the present study are consistent with those reported by Ealo et al. 2016[1]. Specifically, at the MSY station (Montseny; a mid-altitude regional background site at 720 m a.s.l.), which is frequently influenced by transported anthropogenic fine particles, the SSAAE parameter becomes positive during non-intense SDEs, resulting in the detection of 50% of SDEs. In contrast, at the more remote, high-altitude MSA station (Montsec; 1570 m a.s.l.), SSAAE successfully identifies approximately 85% of SDEs, while at the JFJ station, located predominantly in the free troposphere, it achieves near-perfect detection (100%). Similar behavior is observed at the DEM station, classified as an urban background site, where the SSAAE < 0 criterion detects, on average, 57% of SDEs. This comparison highlights the limitations of SSAAE in complex, pollution-influenced environments and underscores the importance of incorporating the CV/TV metric derived from OPC measurements for real-time SDE detection, particularly in urban settings where it provides improved overall performance.

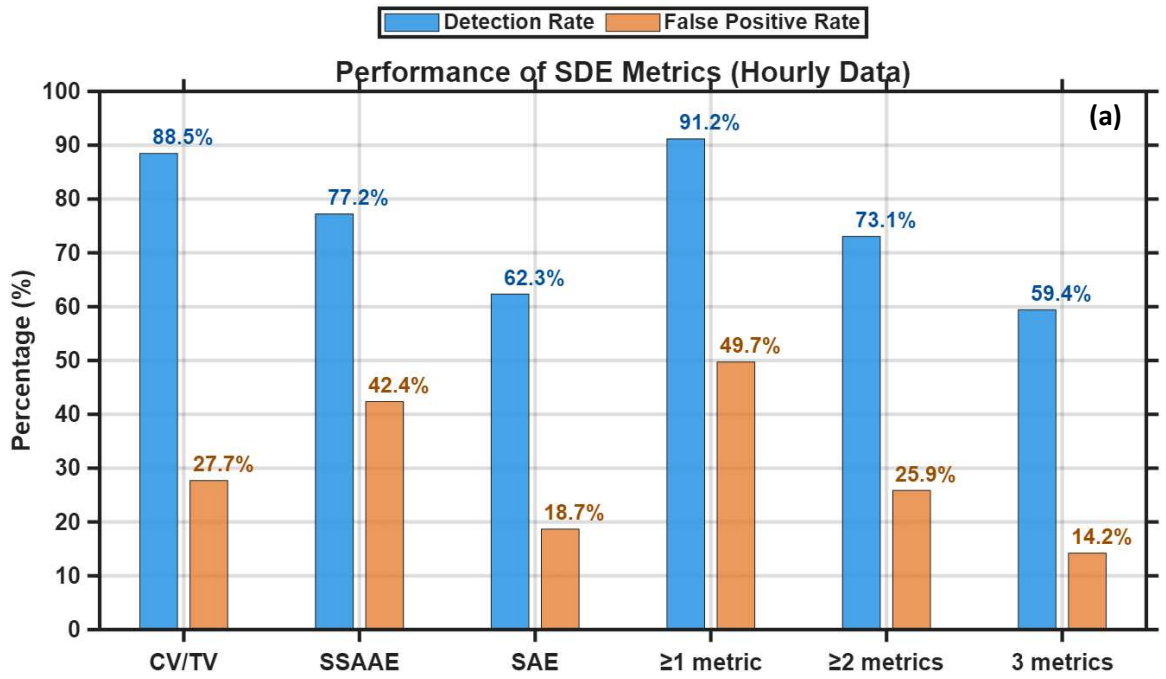
3.4.2 Assessment of SDE detection metrics using XRF-Derived verification

During 2024, a comprehensive evaluation was conducted for all optical criteria previously proposed for SDE detection, i.e. SSAAE < 0, SAE < 1, and CV/TV > 0.70. Number size distributions were measured using a Laser Aerosol Spectrometer (LAS, TSI Model 3340A), which provided an independent particle size distribution dataset. This enabled intercomparison with the

results derived from the Grimm OPC and allowed the assessment of the robustness of the CV/TV criterion across different instruments.

As shown in Figure 6a, the hourly evaluation of the proposed metrics, using SKIRON as the reference dataset for SDE identification, showed detection rates of 88.5%, 77.2%, and 62.3% for CV/TV, SSAAE, and SAE, respectively. The corresponding false positive rates were 27.7%, 42.4%, and 18.7%. These results are consistent with those obtained for the 2015, 2017, and 2020 period (Tables 2–3), although improved performance is observed for the optical metrics. Among the examined metrics, the CV/TV ratio continues to provide a strong balance between sensitivity and specificity, achieving high detection capability with a moderate false positive rate. Among the combined approaches, requiring at least one metric maximizes detection to 91.2% but results in an unacceptably high false-positive rate of 49.7%. Requiring at least two metrics provides a more balanced performance, with an 73.1% detection rate and a 25.6% false-positive rate, whereas requiring all three metrics minimizes false positives to 14.2% but reduces detection to 59.4%.

A closer inspection of this intermediate category shows that the SSAAE and CV/TV pair achieves a detection rate of 72.9% with a false positive rate of 21.0% (Figure 6b). In contrast, dual combinations involving the SAE parameter exhibit more conservative behavior, with the SAE and CV/TV pair minimizing false alarms to 14.2%, albeit at the expense of lower detection efficiency (59.4%). The strict condition requiring all three metrics to be simultaneously satisfied yields the lowest overall false positive rate (14.2%) but also the lowest detection efficiency (59.4%), reflecting a highly conservative classification approach. Overall, these results demonstrate that although multi-metric combinations allow the balance between detection sensitivity and false alarm tolerance to be adjusted, the CV/TV ration alone already achieves a robust and efficient classification, supporting its use as a primary indicator for near-real-time identification of Saharan dust events.



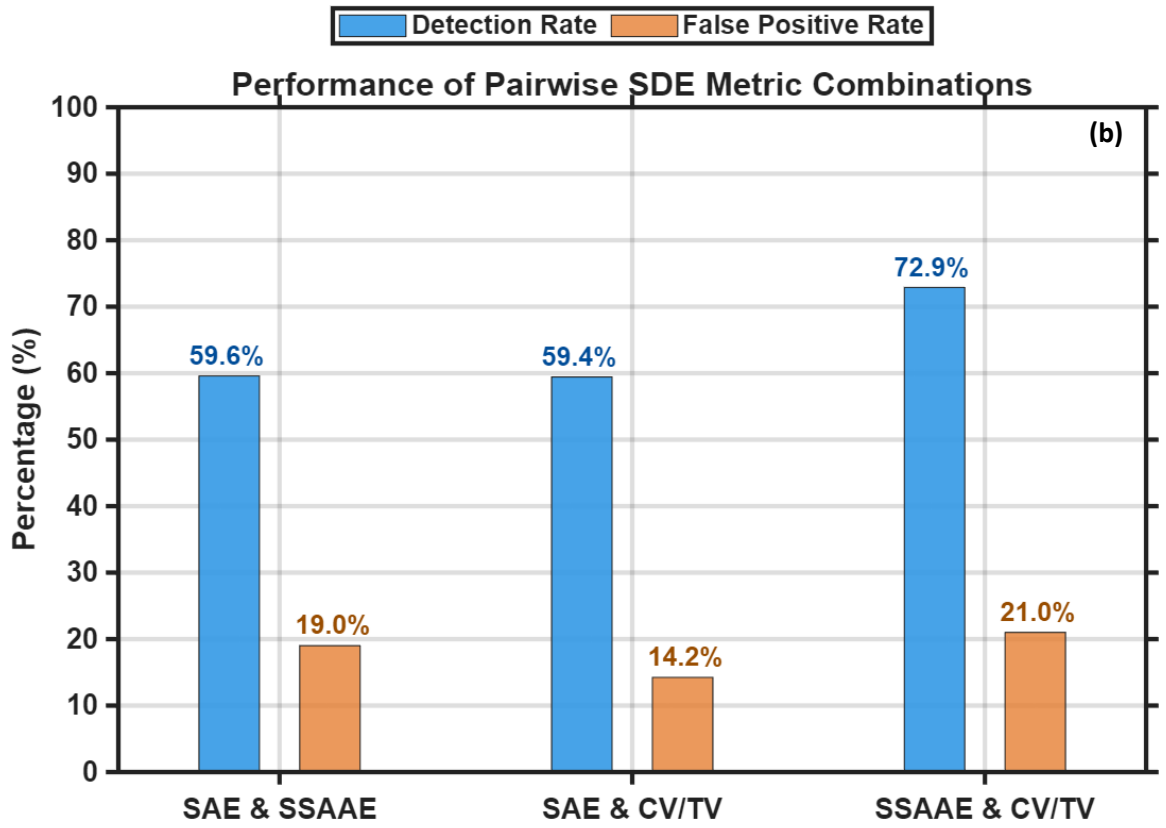


Figure 6. a) Performance of individual and combined SDE detection metrics (CV/TV, SSAAE, SAE) at hourly resolution during 2024, using SKIRON reanalysis as reference (with SDE accounting for 8.9% of the total valid dataset). Detection rates (true positives) and false positive rates are shown for each metric and their combinations (≥1, ≥2, and all three criteria). b) Performance of pairwise SDE detection metric combinations (SAE & SSAAE, SAE & CV/TV, SSAAE & CV/TV) at hourly resolution during 2024, using SKIRON reanalysis as reference. Detection rates (true positives) and false positive rates are shown for each dual-metric constraint.

To further investigate the classification performance of these metrics, the percentage distributions of hourly events classified as correctly detected SDEs (true positives), missed events, correctly identified non-SDE cases (true negatives), and false positive SDE classifications were analyzed for each metric at hourly resolution (Figure 7). The uncertainty band around each decision threshold, defined by the 25th–75th percentile range, was also calculated to account for borderline classifications and measurement variability. For CV/TV, the majority of dust events occur above the 0.70 threshold, while non-SDE cases are concentrated at lower values, with minimal overlap within the uncertainty band. SSAAE exhibits a broader overlap between SDE and non-SDE distributions around the zero threshold, explaining its higher false positive rate. SAE shows a wider spread of detected SDEs extending above the threshold, while non-SDE cases are concentrated at higher values, indicating that SAE provides a more conservative classification and is less sensitive to mixed dust events.

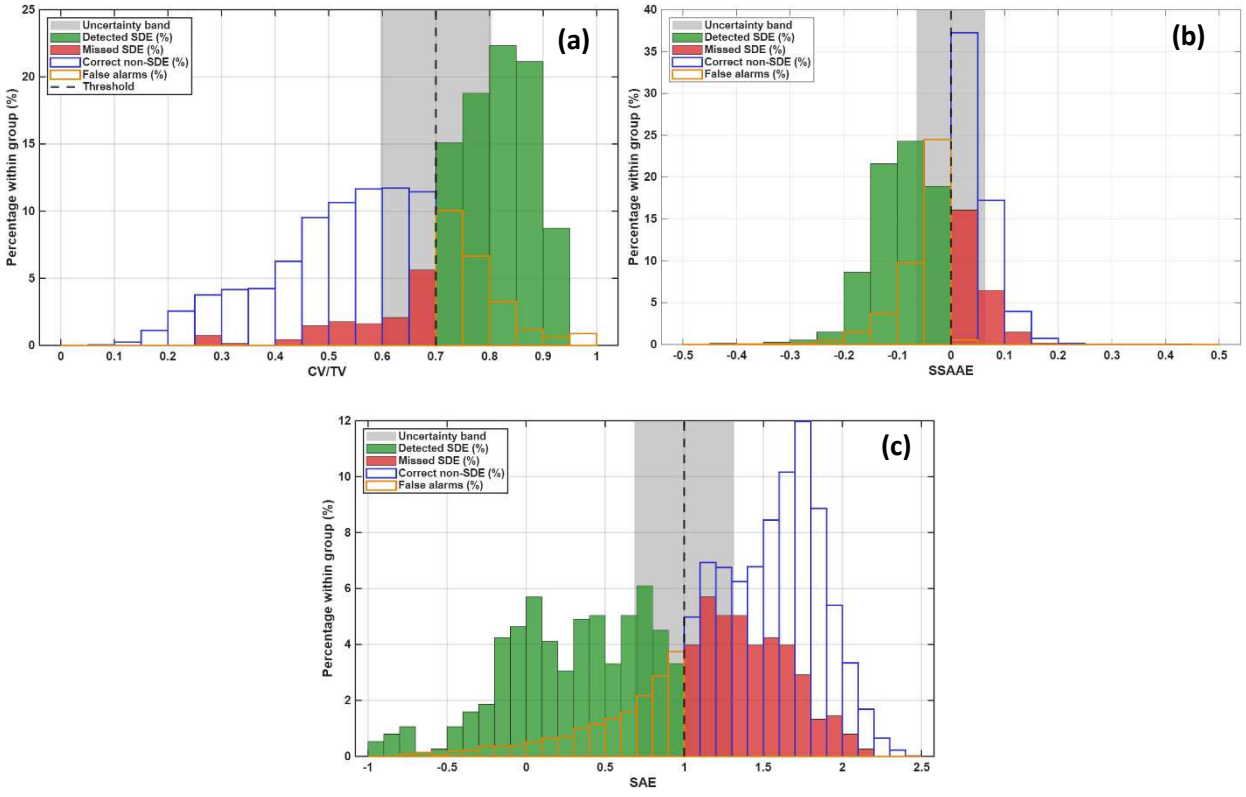
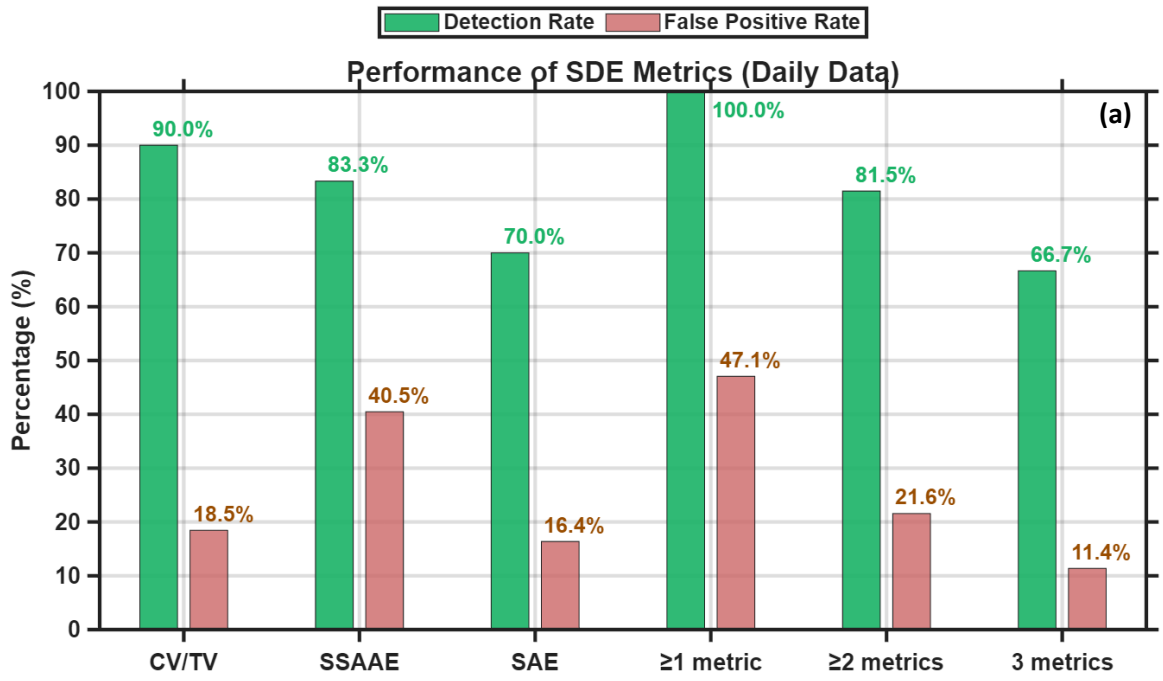


Figure 7. Distribution of hourly values of the SDE detection metrics (CV/TV, SSAAE, and SAE) using SKIRON reanalysis as reference. For each parameter, data are classified into four categories: correctly detected SDEs (true positives), missed SDEs (false negatives), correctly identified non-SDE cases (true negatives), and false alarms (false positives). The vertical dashed lines indicate the applied decision thresholds (CV/TV = 0.70, SSAAE = 0, SAE = 1),

while the shaded regions represent the uncertainty bands around each threshold, accounting for measurement variability and borderline cases.

To further assess the SDE detection efficiency of the studied metrics, a complementary analysis is performed using specific elemental ratios as tracers of SDEs. The presence of SDEs was verified using both SKIRON dust reanalysis data and elemental composition analysis of 24-hour $PM_{2.5}$ filters by energy-dispersive X-ray fluorescence (EDXRF). These elemental tracers, including specific diagnostic elemental ratios, provided additional evidence for the identification of dust-influenced days, consistent with approached proposed in previous studies[39,40,14].

In particular, the Ca/Al and (Ca + Mg)/Fe ratios are used to distinguish between dust originating from different Saharan source regions. Ca/Al ratios above 0.5 are indicative of Saharan dust influence, with higher values typically associated with air masses transported from Tunisia–Algeria compared to those from Libya[41]. The (Ca + Mg)/Fe ratio has also been reported to differ between western and eastern Saharan sources[41,42,40]. Additional elemental ratios, such as Zn/Al and Al/Si, were examined to account for the influence of local and anthropogenic sources; Elevated Zn/Al ratios highlight the contribution of urban and industrial emissions[43], whereas Al/Si ratios above 0.3 are characteristic of desert mineral dust[44]. These elemental ratios, combined with the data from SKIRON model, were used to validate SDE metrics during 2024. Table S1 presents the basic statistics of the elemental metrics under SDE and non-SDE conditions, while Figure 8 shows the performance characteristics of the investigated metrics for SDE and non-SDE classification at daily resolution. In addition, Figure 9 presents the percentage distribution of the event classification for the CV/TV, SSAAE and SAE criteria.



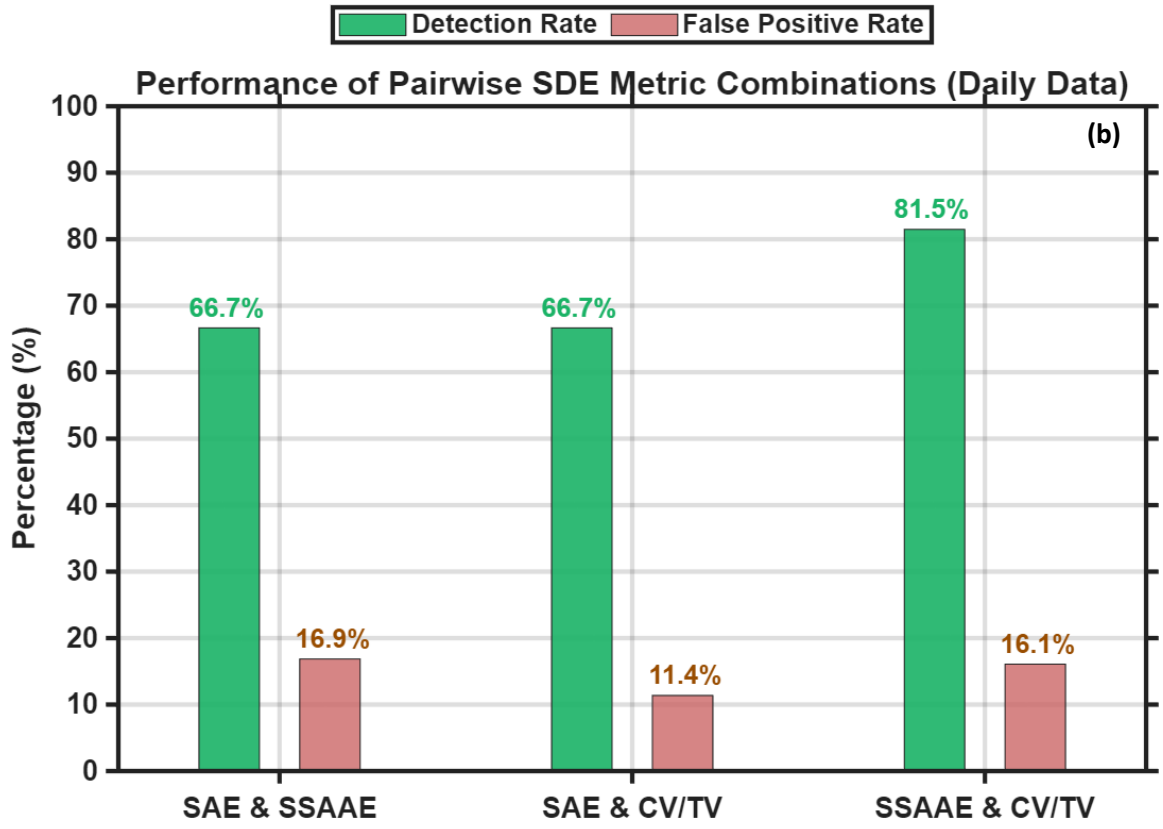


Figure 8. a) Performance of SDE detection metrics (CV/TV, SSAAE, SAE) at daily resolution, considering events confirmed by both SKIRON and XRF elemental analysis. Detection rates (true positives) and false positive rates are shown for each metric and their combinations (≥1, ≥2, and all three criteria). b) Performance of pairwise SDE detection metric combinations (SAE & SSAAE, SAE & CV/TV, SSAAE & CV/TV) at daily resolution, considering events

confirmed by both SKIRON and XRF elemental analysis. Detection rates (true positives) and false positive rates are shown for each dual-metric constraint.

When the performance validation was extended to daily resolution using XRF-based chemical confirmation of SDEs, clearer discrimination among the different event classifications was observed, as shown in Figure 9. For all three metrics, the overlap between the SDE and non-SDE classes was reduced, particularly within the uncertainty bands, likely reflecting the smoothing of short-term variability. CV/TV showed the most distinct discrimination, with SDE cases remaining predominantly above the 0.70 threshold. SSAAE also exhibited more compact distributions, although overlap near the zero threshold persisted, consistent with its sensitivity to mixed aerosol conditions. SAE showed improved discrimination, with most non-SDE cases clearly located above the threshold and SDE cases distributed mainly below or near it.

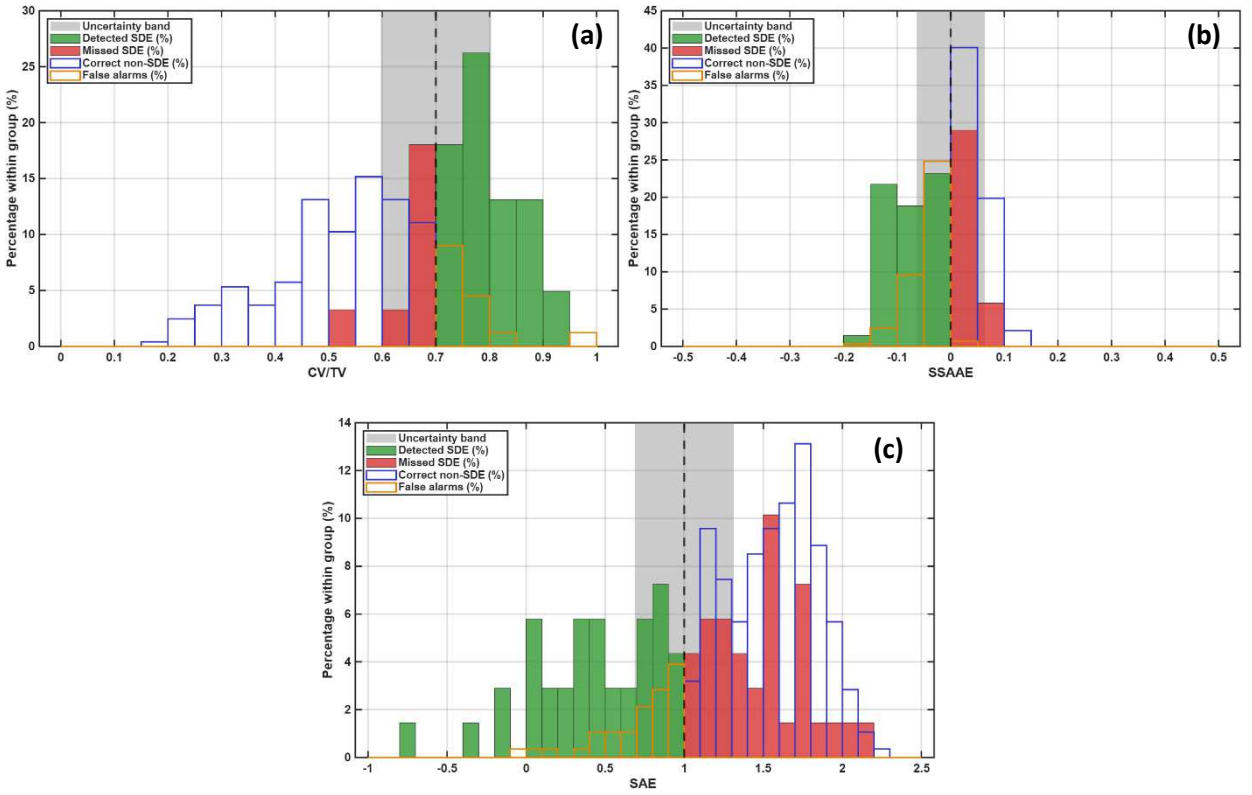


Figure 9. Distribution of daily values of the SDE detection metrics (CV/TV, SSAAE, and SAE) using XRF analysis as reference. For each parameter, data are classified into four categories: correctly detected SDEs (true positives), missed SDEs (false negatives), correctly identified non-SDE cases (true negatives), and false alarms (false positives). The vertical dashed lines indicate the applied decision thresholds (CV/TV = 0.70, SSAAE = 0, SAE = 1), while the shaded regions represent the uncertainty bands around each threshold, accounting for measurement variability and borderline cases.

These distribution patterns are consistent with the higher detection rates obtained using the daily datasets (i.e. 88.0%, 92.0%, and 84.0% for CV/TV, SSAAE, and SAE, respectively) (Figure 8a),

compared with the corresponding results derived from the 1-hour datasets. The benefit of daily XRF-based verification is also evident in the combined-metric analysis, where the SSAAE–CV/TV pair achieved a detection rate of 81.5% while limiting false positives to 16.1% (Figure 8b). By contrast, combinations involving SAE were more restrictive, reducing false positives to 11.4% for SAE–CV/TV but with lower detection efficiency (66.7%). Overall, the daily analysis indicates that temporal averaging combined with independent chemical verification reduces the influence of transient local sources and improves the robustness of SDE classification across metrics.

Overall, the 2024 analysis confirms the robustness and transferability of the SDE detection criteria across independent instruments and temporal resolutions. Among them, the CV/TV ratio emerges as the most reliable indicator, consistently combining high detection efficiency with a comparatively low false positive rate. Although SSAAE and SAE provide useful complementary information, they are more susceptible to uncertainty under mixed urban conditions. To further support the robustness of the proposed CV/TC threshold, a ROC (Receiver Operating Characteristic)-type analysis was performed using the 2024 LAS dataset (Figure S5). The ROC curve illustrates the trade-off between detection efficiency (true positive rate) and false positive rate as a function of the decision threshold, allowing for an objective assessment of classification performance[45]. As shown in Figure S4, the CV/TV = 0.70 threshold lies close to the optimal region of the curve, where high detection rates are achieved with relatively low false positive frequencies. This finding is fully consistent with the statistical and distribution-based analyses presented above, confirming that this threshold provides a well-balanced compromise between sensitivity and specificity across both hourly and daily evaluations.

4. Conclusions

The results demonstrate that Saharan dust events produce a distinct and physically consistent optical–microphysical signature, characterized by enhanced scattering and extinction, reduced SAE and EAE values, negative SSAAE, and a pronounced increase in the coarse-to-total volume ratio (CV/TV). Among the investigated indicators, CV/TV emerged as the most robust and transferable metric for SDE detection. The threshold CV/TV > 0.7 consistently provided high detection efficiency with comparatively low false positive rates across different years, instrument and validation approaches. Overall, the combined optical-microphysical approach provides a

reliable framework for detecting Sahara dust intrusions in complex urban background environments.

The proposed CV/TV > 0.70 threshold is recommended as a primary operational criterion. Used alone, CV/TV achieves the best overall balance between sensitivity and specificity, with a detection rate of 88.5% and a false-positive rate of 27.7%. In contrast, SSAAE alone provides relatively high detection efficiency (77.2%) but produces a substantially higher false-positive rate (42.4%), limiting its suitability as an independent classification criterion. SAE < 1 is more conservative, with a lower false-positive rate of 18.7%, but detects only 62.3% of the identified Saharan dust events. The pairwise analysis shows that SSAAE combined with CV/TV offers the most effective classification, retaining a relatively high detection rate of 72.9%, while reducing the false-positive rate to 21.0%. By comparison, the combination of SAE and CV/TV provides the most conservative filter, with the lowest false-positive rate of 14.2%, although this is accompanied by a lower detection rate of 59.4%.

Beyond event identification, the proposed SDE detection framework may also support atmospheric and climate-related research. By identifying periods influenced by Saharan dust using high-temporal-resolution in situ optical and microphysical measurements, the approach provides an observational basis for examining associated changes in aerosol optical properties relevant to dust radiative effects. The CV/TV-based criterion may therefore be useful for evaluating simulated dust occurrence and associated aerosol optical properties, particularly in regions where satellite retrievals and regional model simulations remain uncertain. Its performance under complex urban-background conditions further indicates its potential for characterizing mixtures of mineral dust and anthropogenic aerosols in the Mediterranean. Following further validation across multiple sites, seasons, and atmospheric conditions, the methodology could contribute to the evaluation of regional dust models and strengthen the observational characterization of mineral-dust effects on atmospheric composition, air quality, and radiative forcing.

DATA AVAILABILITY

The data used in this study were primarily collected from the measurements at the NCSR Demokritos station (DEM station). Most of the data analyzed in this paper are publicly available through the EBAS database at https://ebas.nilu.no/. Supplementary datasets and metadata specific to this study, which are not available through the EBAS portal, have been deposited in Zenodo and are accessible at:

https://doi.org/10.5281/zenodo.17707601 Any additional information can be provided upon reasonable request to the corresponding author.

CODE AVAILABILITY

The code used in this study includes proprietary elements that cannot be made publicly available. Researchers may obtain access to the analysis scripts required to reproduce the results by contacting the corresponding author and entering into appropriate agreements if necessary.

References

1. **Ealo, M. *et al.*** Detection of Saharan dust and biomass burning events using near-real-time intensive aerosol optical properties in the north-western Mediterranean. *Atmos. Chem. Phys.* **16**, 12567–12586 (2016).
2. **Donateo, A. *et al.*** Long-term observations of aerosol optical properties at three GAW regional sites in the Central Mediterranean. *Atmos. Res.* **241**, 104976 (2020).
3. **Tzanis, C. & Varotsos, C. A.** Tropospheric aerosol forcing of climate: A case study for the greater area of Greece. *Int. J. Remote Sens.* **29**, 2507–2517 (2008).
4. **Gkikas, A. *et al.*** Direct radiative effects during intense Mediterranean desert dust outbreaks. *Atmos. Chem. Phys.* **18**, 8757–8787 (2018).
5. **IPCC.** *Climate Change 2013: The Physical Science Basis*. Contribution of Working Group I to the Fifth Assessment Report of the Intergovernmental Panel on Climate Change (Cambridge Univ. Press, Cambridge, 2013).
6. **Kaskaoutis, D. G. *et al.*** Analysis of intense dust storms over the eastern Mediterranean in March 2018: Impact on radiative forcing and Athens air quality. *Atmos. Environ.* **209**, 23–39 (2019).
7. **Collaud Coen, M. *et al.*** Saharan dust events at the Jungfraujoch: detection by wavelength dependence of the single scattering albedo and first climatology analysis. *Atmos. Chem. Phys.* **4**, 2465–2480 (2004).
8. **Viana, M. *et al.*** Natural sources of atmospheric aerosols influencing air quality across Europe. *Sci. Total Environ.* **472**, 825–833 (2014).
9. **Varga, G., Ujvari, G. & Kovacks, J.** Spatiotemporal patterns of Saharan dust outbreaks in the Mediterranean Basin. *Aeolian Res.* **15**, 151–160 (2014).
10. **Escudero, M. *et al.*** Source apportionment for African dust over the Western Mediterranean using the HYSPLIT model. *Atmos. Res.* **99**, 518–527 (2010).
11. **López-Caravaca, A. *et al.*** The impact of intense winter Saharan dust events on PM and optical properties at urban sites in the southeast of the Iberian Peninsula. *Atmosphere* **12**, 1469 (2021).
12. **Vasilatou, V. *et al.*** Long term flux of Saharan dust to the Aegean Sea around the Attica region, Greece. *Front. Mar. Sci.* **4**, 42 (2017).
13. **Escudero, M. *et al.*** A methodology for the quantification of the net African dust load in air quality monitoring networks. *Atmos. Environ.* **41**, 5516–5524 (2007).

14. **Gini, M., Manousakas, M., Karydas, A. G. & Eleftheriadis, K.** Mass size distributions, composition and dose estimates of particulate matter in Saharan dust outbreaks. *Environ. Pollut.* **298**, 118768 (2022).
15. **Diapouli, E. *et al.*** AIRUSE-LIFE +: Estimation of natural source contributions to urban ambient air PM10 and PM2.5 concentrations in southern Europe – Implications to compliance with limit values. *Atmos. Chem. Phys.* **17**, 3673–3685 (2017).
16. **Kinni, P. *et al.*** Health effects of desert dust storm events in the south-eastern Mediterranean: perceptions and practices of local stakeholders. *East. Mediterr. Health J.* **27**, 1092–1101 (2021).
17. **Aghababaeian, H. *et al.*** Global health impacts of dust storms: a systematic review. *Environ. Health Insights* **15**, 16–18 (2021).
18. **Querol, X. *et al.*** Monitoring the impact of desert dust outbreaks for air quality for health studies. *Environ. Int.* **130**, 104867 (2019).
19. **Stafoggia, M. *et al.*** Desert dust outbreaks in Southern Europe: contribution to daily PM10 concentrations and short-term associations with mortality and hospital admissions. *Environ. Health Perspect.* **124**, 413–419 (2016).
20. **Vasilakos, P.N., Upadhyay, A., Manousakas, M.I. *et al.*** Rising dust pollution across Europe in a changing climate. *Nature* **655**, 647–654 (2026). https://doi.org/10.1038/s41586-026-10743-w
21. **Zografou, O. *et al.*** Combined organic and inorganic source apportionment on yearlong ToF-ACSM dataset at a suburban station in Athens. *Atmos. Meas. Tech.* **15**, 4675–4692 (2022).
22. **Eleftheriadis, K. *et al.*** Aerosol microphysics and chemistry reveal the COVID19 lockdown impact on urban air quality. *Sci. Rep.* **11**, 1–11 (2021).
23. **Weingartner, E. *et al.*** Absorption of light by soot particles: determination of the absorption coefficient by means of aethalometers. *J. Aerosol Sci.* **34**, 1445–1463 (2003).
24. **Zanatta, M. *et al.*** A European aerosol phenomenology-5: climatology of black carbon optical properties at 9 regional background sites across Europe. *Atmos. Environ.* **145**, 346–364 (2016).
25. **Kalogridis, A. C. *et al.*** Assessment of wood burning versus fossil fuel contribution to wintertime black carbon and carbon monoxide concentrations in Athens, Greece. *Atmos. Chem. Phys.* **18**, 10219–10236 (2018).
26. **Müller, T., Laborde, M., Kassell, G. & Wiedensohler, A.** Design and performance of a three-wavelength LED-based total scatter and backscatter integrating nephelometer. *Atmos. Meas. Tech.* **4**, 1291–1303 (2011).
27. **Gini, M. *et al.*** Inter-laboratory comparison of ED-XRF/PIXE analytical techniques in the elemental analysis of filter-deposited multi-elemental certified reference materials representative of ambient particulate matter. *Sci. Total Environ.* **780**, 146449 (2021).
28. **Manousakas, M. *et al.*** XRF characterization and source apportionment of PM10 samples collected in a coastal city. *X Ray Spectrom.* 1–11 (2017).
29. **Donateo, A. *et al.*** Characterization of in situ aerosol optical properties at three observatories in the central Mediterranean. *Atmosphere* **9**, 369 (2018).
30. **Pandolfi, M. *et al.*** A European aerosol phenomenology - 6: scattering properties of atmospheric aerosol particles from 28 ACTRIS sites. *Atmos. Chem. Phys.* **18**, 7877–7911 (2018).

31. **Collaud Coen, M. *et al.*** Multidecadal trend analysis of in situ aerosol radiative properties around the world. *Atmos. Chem. Phys.* **20**, 8867–8908 (2020).
32. **Moosmüller, H. *et al.*** Single scattering albedo of fine mineral dust aerosols controlled by iron concentration. *J. Geophys. Res. Atmos.* **117**, 1–10 (2012).
33. **Stein, A. F. *et al.*** NOAA's HYSPLIT atmospheric transport and dispersion modeling system. *Bull. Am. Meteorol. Soc.* **96**, 2059–2077 (2015).
34. **Stohl, A., Forster, C., Frank, A., Seibert, P. & Wotawa, G.** Technical note: the Lagrangian particle dispersion model FLEXPART version 6.2. *Atmos. Chem. Phys.* **5**, 2461–2474 (2005).
35. **Spyrou, C., Mitsakou, C., Kallos, G., Louka, P. & Vlastou, G.** An improved limited area model for describing the dust cycle in the atmosphere. *J. Geophys. Res. Atmos.* **115**, 1–19 (2010).
36. **Granakis, K. *et al.*** Decadal trends for aerosol in-situ optical properties and radiative forcing efficiency in a Mediterranean urban background area. *Atmos. Environ.* (2025).
37. **Eleftheriadis, K. *et al.*** Influence of local and regional sources on the observed spatial and temporal variability of size resolved atmospheric aerosol mass concentrations and water-soluble species in the Athens metropolitan area. *Atmos. Environ.* **97**, 252–261 (2014).
38. **Conte, M. *et al.*** Long-term characterisation of African dust advection in south-eastern Italy: influence on fine and coarse particle concentrations, size distributions, and carbon content. *Atmos. Res.* **233**, 104690 (2020).
39. **Remoundaki, E. *et al.*** PM_{10} composition during an intense Saharan dust transport event over Athens (Greece). *Sci. Total Environ.* **409**, 4361–4373 (2011).
40. **Marconi, M. *et al.*** Saharan dust aerosol over the central Mediterranean Sea: PM_{10} chemical composition and concentration versus optical columnar measurements. *Atmos. Chem. Phys.* **14**, 2039–2054 (2014).
41. **Blanco, A. *et al.*** Characterization of African dust over southern Italy. *Atmos. Chem. Phys.* **3**, 2147–2159 (2003).
42. **Scheuvens, D. *et al.*** Bulk composition of northern African dust and its source sediments—a compilation. *Earth Sci. Rev.* **116**, 170–194 (2013).
43. **Fu, Y. *et al.*** Estimating chemical composition of atmospheric deposition fluxes. *Atmos. Meas. Tech.* **10**, 4389–4401 (2017).
44. **Kopanakis, I. *et al.*** Ambient particulate matter concentration levels and their origin during dust event episodes in the eastern Mediterranean. *Aerosol Sci. Eng.* **2**, 61–73 (2018).
45. **Fawcett, T**. An introduction to ROC analysis. Pattern Recognit. Lett. 27, 861–874 (2006).

ACKNOWLEDGEMENTS

This work was supported by the Action titled "National Network on Climate Change and its Impacts - Climpact", funded by the Public Investment Program of Greece, General Secretariat of Research and Innovation/Ministry of Development and Investments". Partly supported by European Union's Horizon 2020 research and innovation programme under RI-URBANS project GA No 101036245.

COMPETING INTERESTS

All authors declare no financial or non-financial competing interests.

684

685 **Table 1.** Annual and overall statistics (mean and standard deviation) for all Angstrom exponents and CV/TV ratios
686 under SDE and nSDE conditions.

Year	SDEs (%)	SAE SDE	SAE nSDE	AAE SDE	AAE nSDE	AAE370_ 590 SDE	AAE370_ 590 nSDE	EAE SDE	EAE nSDE	SSAAE SDE	SSAAE nSDE	CV/TV (OPC) SDE	CV/TV (OPC) nSDE
2015	3.9	0.77 ± 0.49	1.65± 0.43	1.34± 0.12	1.37± 0.12	1.55±0.21	1.49±0.18	0.80± 0.50	1.66± 0.46	-0.02± 0.04	0.02± 0.06	0.70± 0.14	0.33± 0.20
2017	6.2	0.63 ± 0.26	1.69± 0.35	1.26± 0.09	1.28± 0.12	1.49±0.17	1.36±0.20	0.66± 0.21	1.63± 0.34	-0.02± 0.05	0.04± 0.05	0.78± 0.05	0.44± 0.18
2020	4.5	1.35 ± 0.33	1.99± 0.45	1.24± 0.12	1.32± 0.11	1.37±0.21	1.35±0.18	1.29± 0.30	1.85± 0.41	0.01± 0.04	0.06± 0.07	0.71± 0.09	0.42± 0.15
Average	4.9	0.91 ±0.36	1.78± 0.41	1.28± 0.11	1.32± 0.12	1.47±0.20	1.40±0.19	0.91± 0.34	1.71± 0.40	-0.01± 0.04	0.04± 0.06	0.73± 0.09	0.39± 0.17

687

688 **Table 2.** True positive rates for individual and combined metrics over the entire study period.

Year	SSAAE<0	SAE<1	CV/TV>0.70	At least 1	At least 2	All criteria
2015	61%	49%	76%	80%	58%	48%
2017	57%	47%	85%	94%	56%	39%
2020	53%	25%	77%	81%	50%	24%
Total	57%	57%	80%	85%	55%	40%

689

690 **Table 3.** False positive rates for individual and combined metrics over the entire study period.

Year	SSAAE<0	SAE<1	CV/TV>0.70	At least 1	At least 2	All criteria
2015	31%	11%	16%	38%	15%	4%
2017	38%	22%	32%	55%	28%	9%
2020	17%	8%	13%	23%	12%	4%
Total	29%	14%	20%	39%	18%	6%

691

692

693

694

Supplementary Files

This is a list of supplementary files associated with this preprint. Click to download.

- LongtermassessmentofSaharanDustEventsintheEasternMediterraneanbyOpticalandMicrophysicalAerosolMetricssupplement.docx